



A STATISTICAL STUDY OF THE AVERAGE IRON CHARGE STATE DISTRIBUTIONS INSIDE MAGNETIC CLOUDS FOR SOLAR CYCLE 23

H. Q. SONG¹, Z. ZHONG¹, Y. CHEN¹, J. ZHANG², X. CHENG³, L. ZHAO⁴, Q. HU⁵, AND G. LI⁵

¹ Shandong Provincial Key Laboratory of Optical Astronomy and Solar-Terrestrial Environment, and Institute of Space Sciences, Shandong University, Weihai, Shandong 264209, China; hqsong@sdu.edu.cn

² School of Physics, Astronomy and Computational Sciences, George Mason University, Fairfax, VA 22030, USA

³ School of Astronomy and Space Science, Nanjing University, Nanjing, Jiangsu 210093, China

⁴ Department of Atmospheric, Oceanic, and Space Sciences, University of Michigan, Ann Arbor, MI 48105, USA

⁵ Department of Space Science and CSPAR, University of Alabama in Huntsville, Huntsville, AL 35899, USA

Received 2015 September 25; accepted 2016 April 11; published 2016 June 8

ABSTRACT

Magnetic clouds (MCs) are the interplanetary counterparts of coronal magnetic flux ropes. They can provide valuable information regarding flux rope characteristics at their eruption stage in the corona, which is unable to be explored in situ at present. In this paper, we make a comprehensive survey of the average iron charge-state ($\langle Q \rangle_{\text{Fe}}$) distributions inside 96 MCs for solar cycle 23 using *Advanced Composition Explorer* (ACE) data. Since the $\langle Q \rangle_{\text{Fe}}$ in the solar wind are typically around 9+ to 11+, the Fe charge state is defined as being high when the $\langle Q \rangle_{\text{Fe}}$ is larger than 12+, which implies the existence of a considerable amount of Fe ions with high charge states (e.g., $\geq 16+$). The statistical results show that the $\langle Q \rangle_{\text{Fe}}$ distributions of 92 (~96%) MCs can be classified into four groups with different characteristics. In group A (11 MCs), the $\langle Q \rangle_{\text{Fe}}$ shows a bi-modal distribution with both peaks being higher than 12+. Group B (4 MCs) presents a unimodal distribution of $\langle Q \rangle_{\text{Fe}}$, with its peak being higher than 12+. In groups C (29 MCs) and D (48 MCs), the $\langle Q \rangle_{\text{Fe}}$ remains higher and lower than 12+ throughout ACE's passage through the MC, respectively. Possible explanations of these distributions are discussed.

Key words: magnetic reconnection – Sun: coronal mass ejections (CMEs) – Sun: flares

1. INTRODUCTION

Coronal mass ejections (CMEs) are the most energetic eruptions in the solar system. After CMEs propagate into interplanetary space, they are called interplanetary coronal mass ejections (ICMEs), which can cause geomagnetic activities and affect satellites, power grids, and GPS navigation systems when they interact with the geo-magnetosphere (Gosling et al. 1991; Zhang et al. 2003, 2007). ICMEs are extensively investigated by the solar/space physics community (Gopalswamy 2006; Jian et al. 2006; Kilpua et al. 2013; Chi et al. 2015) for their important role in space weather studies. Magnetic clouds (MCs, Burlaga et al. 1981), large interplanetary magnetic flux rope structures embedded in ICMEs, are more attractive, as they usually cause stronger geomagnetic storms compared to ICMEs without MCs (Lepping et al. 2011, 2015; Wu & Lepping 2011, 2015), and also because they have relatively regular magnetic structures and can be fitted with flux rope reconstruction methods (Lepping et al. 1990; Hu & Sonnerup 2002; Wang et al. 2015).

By investigating the properties of MCs with in situ observations, one can infer the flux rope formation and eruption processes in the corona. However, most MC parameters, e.g., the density, temperature, velocity, volume, and morphology, as well as magnetic field strength, will experience large variation during the propagation from near the Sun to 1 au, due to their expansion, acceleration/deceleration, and interaction with other interplanetary structures. This complicates efforts to investigate the flux rope formation and eruption in the corona through in situ data.

Fortunately, the charge states of ions inside MCs are frozen before the flux ropes leave the corona (e.g., Rakowski et al. 2007; Ko et al. 2010; Gruesbeck et al. 2011; Lynch et al. 2011; Lepri et al. 2012) and therefore they may reflect

their evolution history near the Sun. Usually, the appearance of high ionic charge states implies high electron temperatures and is attributed to magnetic reconnection occurring along the current sheet connecting the flux rope to flare loops (Bemporad et al. 2006; Ko et al. 2013; Song et al. 2015b, 2015c). As reconnection continues toward higher altitude, the flux rope will be added with more layers consisting of reconnected magnetic field lines. And the heated plasma will correspondingly fill in the flux rope structure along these field lines, giving rise to an onion-layer morphology (Ko et al. 2013). Therefore, high ionic charge states inside MCs may provide direct signatures of reconnection in the post-CME current sheet, which are very helpful for addressing some important unresolved issues of CMEs.

One heated debate associated with CMEs is whether the flux ropes exist prior to the eruption or if they are formed during the eruption (Song et al. 2014a, and the references therein). Some numerical simulations (Chen 1996; Lin & Forbes 2000) and observations (Zhang et al. 2012; Cheng et al. 2013, 2014; Patsourakos et al. 2013; Song et al. 2014b, 2015b) support the notion that flux ropes can exist prior to the eruption, while other simulations (Mikić & Linker 1994) and observations (Song et al. 2014a; Ouyang et al. 2015) demonstrate that flux ropes can also be formed during the eruption. When the eruption involves a pre-existing flux rope with relatively low temperature, surrounded by heated plasmas formed through magnetic reconnection in the current sheet, we would expect to detect an MC with a low-ionization-state center and high-ionization-state shell (Lin et al. 2004; Ko et al. 2013; Song et al. 2015b). On the contrary, when the flux rope is mostly formed during the eruption, a more ionized center might be observed due to stronger heating and higher densities at lower heights (Ko et al. 2013). It has been reported that the [Fexviii]

line intensity in the post-CME current sheet decreases with height, supporting this suggestion (Ciaravella et al. 2013).

Iron is an astrophysically abundant heavy element. Its heavy mass allows the iron ions, detected in situ, to be well-separated from other abundant heavy ions in the normal solar wind and ICMEs due to significantly less interference from other species. This is because ions are distinguished based on their mass and charge (mass/charge) by present instruments (Gloeckler et al. 1998; von Steiger et al. 2000). It has been suggested that Fe ions are more affected by the continuing heating along a more extended space of the plasma flow near the Sun, and other species such as C and O ions are mainly sensitive to the heating processes at the earlier stage (e.g., Ko et al. 2010; Gruesbeck et al. 2011; Lepri et al. 2012). Therefore, the in situ charge states of different ion species cannot be compared with each other in a straightforward manner. Here we focus our study on Fe ions. Average Fe charge states ($\langle Q \rangle_{\text{Fe}}$) in the solar wind are typically around 9+ to 11+ (e.g., Lepri et al. 2001). Based on comparisons of charge-state distributions between the normal solar wind and ICMEs with high Fe charge states, Lepri & Zurbuchen (2004) determined a reasonable threshold of $\langle Q \rangle_{\text{Fe}}$ as 12+, above which it implies a considerable amount of high Fe charge states in ICMEs and vice versa. High Fe charge states above this threshold have been observed in over 50% ICMEs, therefore this threshold has been used as one complementary identifier of ICMEs (Lepri et al. 2001; Lepri & Zurbuchen 2004). However, a comprehensive analysis of the $\langle Q \rangle_{\text{Fe}}$ distribution inside MCs has not yet been performed.

In this paper, we make a comprehensive survey of $\langle Q \rangle_{\text{Fe}}$ distributions of 96 MCs for solar cycle 23 using *ACE* data and ~96% of them (92 MCs) can be classified into four groups, shedding more light on the flux rope formation process. The instruments are introduced in Section 2, and the data analysis is presented in Section 3. Section 4 provides possible explanations of the results, followed by a summary in Section 5.

2. INSTRUMENTS

The Fe charge state is obtained using the Solar Wind Ion Composition Spectrometer (SWICS, Gloeckler et al. 1998) on board the *Advanced Composition Explorer* (*ACE*), which launched in 1997 and orbits around the L1 point. As a mass spectrometer, SWICS consists of a time-of-flight (TOF) system and an energy resolving solid-state detector (SSD). The TOF system measures the speed of each ion and the SSD determines its residual energy, which allows the determination of the mass, charge, and energy of the detected ion. SWICS can determine the density, bulk speed, and the thermal speed of almost 40 heavy ions and provide the charge-state distributions and abundances of ~10 elements (also see Lepri et al. 2001). In this study, we use the newly released SWICS 1.1 level 2 data, which are calculated by an improved calibration algorithm and have a better accuracy than the previous versions (Shearer et al. 2014). The process for removing accidental coincidence events has been improved, leading to an increase in the identification of rare ions such as Fe^{6+} and Fe^{7+} . Except for the ionic charge state, we also use the data from MAG (Smith et al. 1998) and SWEPM (McComas et al. 1998) on board *ACE* for the magnetic field and plasma measurements of associated MCs.

3. DATA ANALYSIS

MCs in the solar wind can be identified if the magnetic field strength is higher than the surrounding background, the field direction rotates smoothly through a large angle, and the proton temperature is lower compared to the environment (Burlaga et al. 1981). In this study, we choose to use the MC lists published by other authors, instead of examining MCs by ourselves. This separates issues related to the MC identification and to the ionic charge-state analysis, making our study more focused. As no unique and fully objective way has been developed to identify MCs in interplanetary space (e.g., Huttunen et al. 2005), some subjective judgements may influence the decision on whether a candidate is an MC or not, as well as exact locations of its front and back boundaries. Therefore, some disagreements on MC boundary locations often exist among different MC lists. We will discuss how this may affect our statistical results in Section 4.

3.1. MC Lists

The public 1-h resolution $\langle Q \rangle_{\text{Fe}}$ data from SWICS have been available on the website of the *ACE* science center since 1998 February (<http://www.srl.caltech.edu/ACE/ASC/index.html>), so we include the MCs detected at L1 between 1998 February and 2009 December in this survey. Two MC lists are used here; one is published by Huttunen et al. (2005) and includes MCs analyzed with *WIND* data in 1998 February at the L1 point and 60 MCs analyzed with *ACE* data from 1998 March to 2003 December (See Table 2 of their paper). The other list is from the *WIND* MFI team, which provided MCs from 1995 February to 2009 December (http://wind.nasa.gov/mfi/mag_cloud_S1.html; Lepping & Wu 2010), including 38 MCs from 2004 to 2009 observed at the L1 point. Note that the *WIND* spacecraft did not always orbit around L1 from 1994 to 2003, so we did not use its MC information between 1998 and 2003. In total, with the above two lists we acquired 100 MCs from 1998 February to 2009 December at the L1 point. Among them, 96 MCs have complete Fe charge-state data as recorded by SWICS, and 2/2 MCs have incomplete/no Fe charge-state data. The typical scale of MC structures is around 0.25 au (e.g., Lepping et al. 2006), ~5900 Earth radii (R_E), and the average duration of MCs is close to 20 hr (Wu & Lepping 2011, 2015). When both *WIND* and *ACE* are around the L1 point, their separation distance is mostly along the radial direction and generally less than 240 R_E , so except for a time delay of several tens of minutes, their plasma and magnetic field measurements are almost identical. In some cases, there is a lateral separation of about 200 R_E along the east–west direction, which is still significantly smaller than the typical size of the MC near 1 au, and not considerable. We compared the *WIND* and *ACE* measurements for each MC from 2004 to 2009 and confirmed this point. Therefore, the magnetic field measurement by *WIND* and the charge-state measurement by *ACE* can be used together for the purposes of our study.

3.2. Criteria and Statistical Results

Following Lepri & Zurbuchen (2004), the $\langle Q \rangle_{\text{Fe}}$ higher/lower than 12+ is defined as the high/normal charge state. With this threshold, we found that there are 50 MCs that contain a high charge state and 48 MCs that do not. This is consistent with the ICME percentage associated with high Fe charge state as reported by Lepri et al. (2001) and Lepri &

Zurbuchen (2004). In Figure 1, the histograms display the yearly total number of MCs. The blue/red portions of the bars correspond to MCs without/with high charge state. The line connected by black filled circles shows the yearly sunspot number. Figure 1 shows that the high Fe charge-state MCs present in the rising (1998–1999), maximum (2000), and

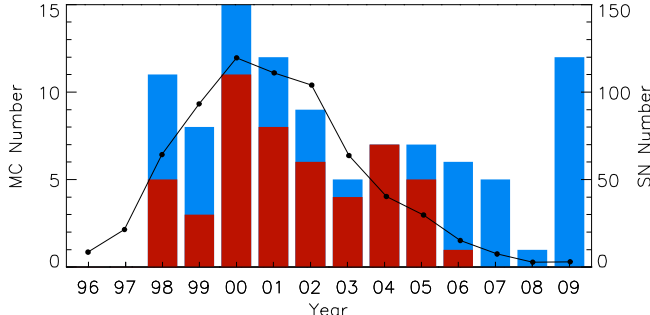


Figure 1. Yearly number of MCs in the study. The blue/red portions of the bars correspond to the MCs without/with a high Fe charge state. The line connected by filled circles shows the yearly sunspot number.

declining (2001–2005) phases of solar cycle 23, and almost no high Fe charge-state MCs are observed in the past solar minimum (2006–2009).

After inspecting the $\langle Q \rangle_{\text{Fe}}$ distributions inside the 96 MCs with complete Fe charge-state data from SWICS, we find that $\sim 96\%$ of them (92 MCs) can be divided into four groups (A, B, C, and D) based on their distribution characteristics. The remaining four MCs are included in Group E, which will be discussed later. Table 1 lists the MC durations in every group according to their time sequence. A summary of the classification results is presented in the diagram of Figure 2.

To illustrate the $\langle Q \rangle_{\text{Fe}}$ distribution characteristics inside MCs for Groups A–D, we select one representative event from each group, and plot their corresponding observations of the magnetic field, plasma, and Fe charge state in Figures 3–6. Panel (a) presents the total magnetic field strength (black line) and the three components, which are plotted in the Geocentric Solar Ecliptic coordinate. The red, green, and blue lines correspond to the X, Y, and Z components, respectively. The solar wind speed, density, and temperature are presented in

Table 1
Classification Groups (G) and Their MCs at the L1 Point for Solar Cycle 23

G	MC Start-End Time (UT) yy mm dd-mm dd hh:mm	MC Start-End Time (UT) yy mm dd-mm dd hh:mm	MC Start-End Time (UT) yy mm dd-mm dd hh:mm
A	1998 Oct 19 04:00–Oct 20 06:00	1999 Apr 16 20:00–Apr 17 18:00	1999 Apr 21 12:00–Apr 22 13:00
	2000 Aug 12 05:00–Aug 13 02:00	2000 Nov 06 22:00–Nov 07 15:00	2001 Mar 19 22:00–Mar 21 23:00
	2001 May 28 11:00–May 29 06:00	2001 Nov 24 17:00–Nov 25 13:00	2002 Apr 17 24:00–Apr 19 01:00
	2003 Aug 18 06:00–Aug 19 11:00	2004 Nov 09 20:54–Nov 10 03:24	
		2003 Mar 20 13:00–Mar 20 22:00	2004 Aug 29 18:42–Aug 30 20:48
B	2001 Mar 04 16:00–Mar 05 02:00		
B	2005 Dec 31 14:48–Jan 01 10:48		
C	1998 Jun 24 12:00–Jun 25 16:00 ^a	1998 Sep 25 08:00–Sep 26 12:00 ^a	1999 Feb 18 14:00–Feb 19 11:00
C	2000 Feb 12 12:00–Feb 12 24:00	2000 Feb 21 14:00–Feb 22 12:00 ^a	2000 Jul 11 23:00–Jul 13 02:00
C	2000 Jul 15 05:00–Jul 15 14:00	2000 Jul 15 19:00–Jul 16 12:00	2000 Sep 17 23:00–Sep 18 14:00
C	2000 Oct 13 17:00–Oct 14 13:00	2001 Mar 27 22:00–Mar 28 05:00	2001 Apr 12 10:00–Apr 13 06:00
C	2001 Apr 28 24:00–Apr 29 13:00	2001 Oct 03 01:00–Oct 03 16:00	2002 Feb 28 18:00–Mar 01 10:00
C	2002 Mar 19 22:00–Mar 20 10:00 ^a	2002 Mar 24 10:00–Mar 25 12:00 ^a	2002 Apr 20 13:00–Apr 21 15:00 ^a
C	2003 Oct 29 12:00–Oct 30 01:00 ^a	2003 Nov 20 11:00–Nov 21 01:00	2004 Apr 04 02:48–Apr 05 14:48
C	2004 Jul 22 15:24–Jul 22 23:06 ^a	2004 Jul 24 12:48–Jul 25 13:18	2004 Nov 08 03:24–Nov 08 16:36 ^a
C	2004 Nov 10 03:24–Nov 10 11:06	2005 May 15 05:42–May 15 22:18	2005 May 20 07:18–May 21 05:18 ^a
C	2005 Jun 12 15:42–Jun 13 07:06 ^a	2006 Dec 14 22:48–Dec 15 19:48	
D	1998 Feb 04 05:00–Feb 05 14:00	1998 Feb 17 10:00–Feb 18 04:00	1998 Mar 04 15:00–Mar 05 21:00
D	1998 Jun 02 10:00–Jun 02 16:00	1998 Aug 20 08:00–Aug 21 18:00 ^b	1998 Nov 13 04:00–Nov 14 06:00
D	1999 Mar 25 16:00–Mar 25 23:00	1999 Aug 09 10:00–Aug 10 14:00	1999 Aug 22 12:00–Aug 23 06:00
D	1999 Sep 21 20:00–Sep 22 11:00	1999 Nov 14 01:00–Nov 14 09:00	2000 Jul 13 15:00–Jul 13 24:00
D	2000 Jul 31 22:00–Aug 01 12:00	2000 Aug 10 20:00–Aug 11 08:00	2000 Oct 03 15:00–Oct 04 14:00 ^b
D	2001 Apr 21 23:00–Apr 22 24:00	2001 Jun 18 23:00–Jun 19 14:00	2001 Jul 10 17:00–Jul 11 23:00
D	2001 Oct 31 22:00–Nov 01 18:00	2002 May 19 04:00–May 19 22:00	2002 Aug 02 06:00–Aug 02 22:00
D	2002 Sep 30 23:00–Oct 01 15:00	2003 Jan 27 01:00–Jan 27 15:00 ^b	2003 Jul 17 15:18–Jul 18 03:48
D	2005 Oct 31 02:54–Oct 31 20:24	2006 Feb 05 19:06–Feb 06 13:06	2006 Apr 13 14:48–Apr 13 20:48 ^b
D	2006 Apr 13 20:36–Apr 14 09:54	2006 Aug 30 21:06–Aug 31 14:54	2006 Sep 30 08:36–Sep 30 21:36
D	2007 Jan 14 14:06–Jan 15 06:54	2007 Mar 24 03:06–Mar 24 16:54	2007 May 21 22:54–May 22 13:36
D	2007 Nov 19 23:24–Nov 20 12:54	2007 Dec 25 15:42–Dec 26 06:48	2008 Dec 17 03:06–Dec 17 14:24
D	2009 Jan 02 06:06–Jan 02 15:06 ^b	2009 Feb 04 00:06–Feb 04 10:54	2009 Mar 12 00:42–Mar 13 00:42
D	2009 Jun 27 15:18–Jun 28 18:18	2009 Jul 21 03:54–Jul 21 17:06	2009 Sep 10 10:24–Sep 10 16:24
D	2009 Sep 30 07:54–Sep 30 16:54	2009 Oct 12 12:06–Oct 12 16:48	2009 Oct 17 22:06–Oct 18 07:24
D	2009 Oct 29 05:12–Oct 29 22:48	2009 Nov 01 08:48–Nov 02 07:48	2009 Dec 12 19:48–Dec 14 05:18
E	1998 May 02 12:00–May 03 17:00	1998 Nov 08 23:00–Nov 10 01:00	2000 Oct 28 24:00–Oct 29 23:00
E	2005 Jun 15 05:48–Jun 16 07:48		

Notes.

^a With one or a few data points lower than 12+.

^b With one or a few data points higher than 12+.

panels (b)–(d) sequentially. Panel (e) is the Fe charge-state distribution, and the last panel is the $\langle Q \rangle_{\text{Fe}}$ in which the horizontal purple dotted line marks the level of 12+. The

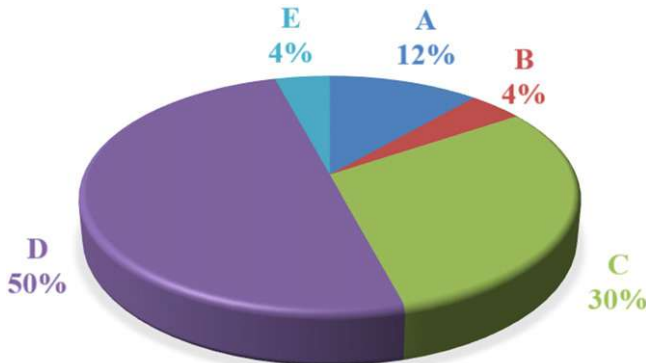


Figure 2. Diagram showing the percentages of different groups for the 96 MCs with complete Fe charge-state data.

locations of the ICME shock (if it exists) and MC boundaries are depicted with the purple vertical solid line and dot-dashed lines, respectively.

In Group A (11 MCs), the $\langle Q \rangle_{\text{Fe}}$ inside MCs presents a bimodal distribution with two peaks that are higher than 12+ and less than 12+ between the peaks, as shown in Figure 3(f). It is obvious that a considerable amount of high Fe charge states ($\sim 16+$) appear in this event (Figure 3(e),) resulting in the elevated $\langle Q \rangle_{\text{Fe}}$. Group B (4 MCs) is defined by the $\langle Q \rangle_{\text{Fe}}$ inside MCs showing a unimodal distribution with its peak higher than 12+, as shown in Figure 4(f). Note that the $\langle Q \rangle_{\text{Fe}}$ on either side of the peak is lower than 12+. In Group C (29 MCs), the $\langle Q \rangle_{\text{Fe}}$ remains higher than 12+ during ACE's passage through the MC, as shown in Figure 5(f). Figure 5(e) shows that this event is always associated with lots of Fe charge states as high as $\geq 16+$, and the enhancement of high Fe charge states is almost coincident with the passage of the MC. Note that the MC $\langle Q \rangle_{\text{Fe}}$ in Group C can have a broad variation (e.g., $13+ \sim 16+$) with different patterns. In this study, we do

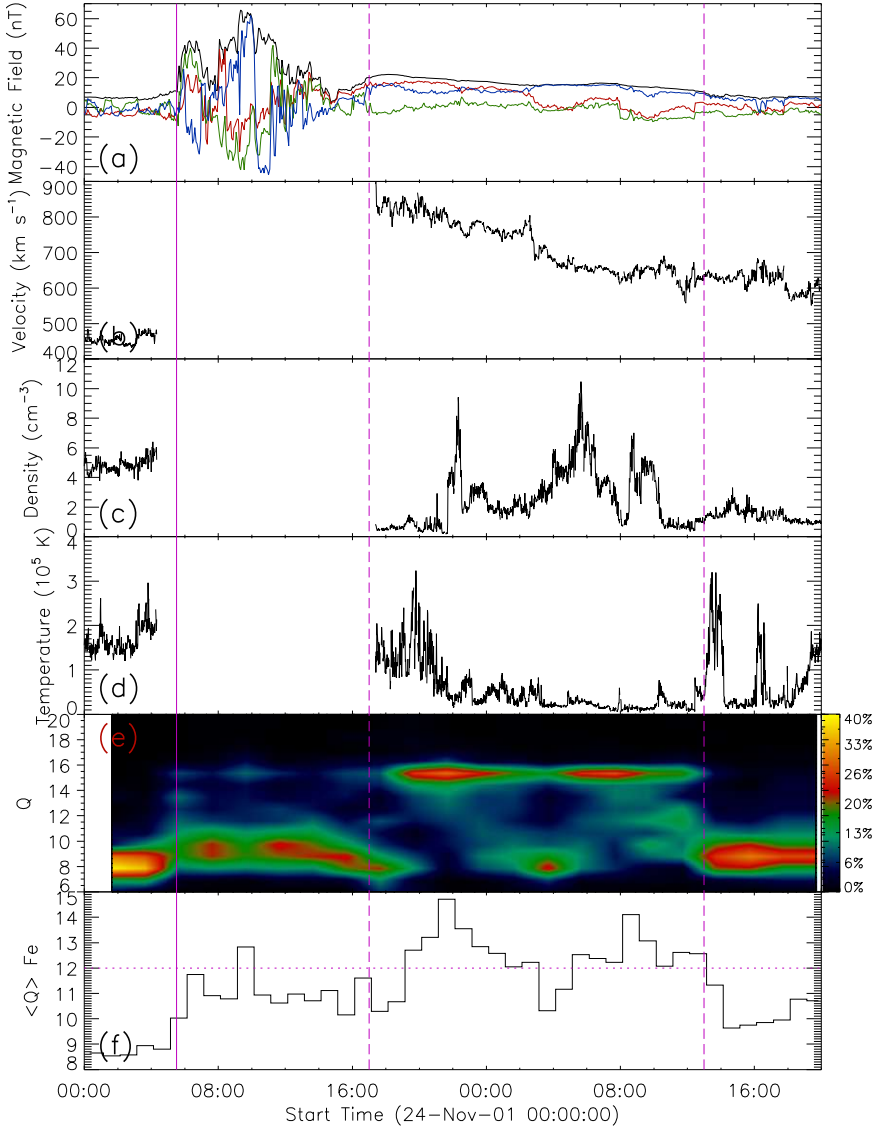


Figure 3. Solar wind parameters and charge-state distribution measured with ACE for the 20011124 event in Group A. (a) The total magnetic field strength (black line) and the X (red), Y (green), and Z (blue) components in the GSE coordinate; (b)–(d) the bulk speed, density, and temperature of the solar wind; (e) the Fe charge-state-distribution map; and (f) the $\langle Q \rangle_{\text{Fe}}$. The horizontal purple dotted line marks the level of 12+. The locations of the ICME shock and MC boundaries are depicted with the purple vertical solid line and the dot-dashed lines, respectively.

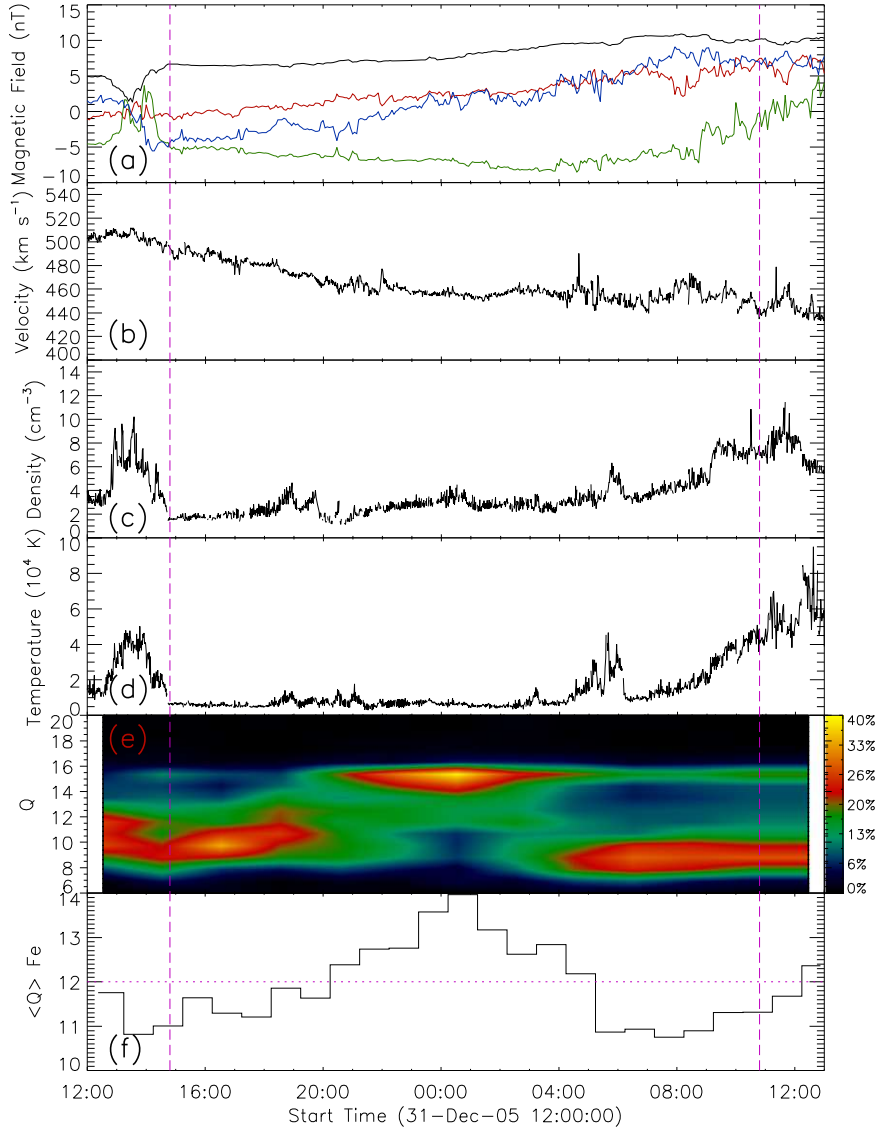


Figure 4. Same as Figure 3, but for the 20051231 event in Group B.

not distinguish these pattern details and classify them into one single group, since we are mainly interested in the appearance of a considerable amount of Fe ions with high charge states, which is defined as when the $\langle Q \rangle_{\text{Fe}}$ is over 12+ (Lepri et al. 2001), and higher $\langle Q \rangle_{\text{Fe}}$ values simply indicating high charge state Fe ions are more abundant. Group D (48 MCs) includes MCs that are not associated with high charge states, i.e., with $\langle Q \rangle_{\text{Fe}}$ less than 12+, as presented in Figure 6. Again, the MC $\langle Q \rangle_{\text{Fe}}$ in Group D may have some variation as well (e.g., 9+ \sim 11+), but it is not of interest here.

Panels (e) in Figures 3–6 clearly show that when the $\langle Q \rangle_{\text{Fe}}$ is larger than 12+, a considerable amount of ions with charge states even higher than 16+ are frequently present. Accordingly, we find that the variation trend of $\langle Q \rangle_{\text{Fe}}$ is in general consistent with that of the $\text{Fe}^{>16+}$ abundance (i.e., $\text{Fe}^{>16+}/\text{Fe}_{\text{total}}$, not included here), which is often used as a measure of the unusually enhanced charge states (e.g., Lepri et al. 2001). This supports the notion that the prescribed threshold of 12+ is an appropriate criterion to represent the presence of a considerable amount of high Fe charge states, which can be further verified by checking the complete Fe

charge-state distributions and $\langle Q \rangle_{\text{Fe}}$ variations (cyan) within all MCs in Groups A–D, as shown in Figure 7. The horizontal white dotted line in each panel marks the level of 12+ for $\langle Q \rangle_{\text{Fe}}$. Note that only the MC part of the data is plotted, with the left/right boundary of each panel being the MC start/end time. It is seen that the Fe charge-state distributions present an obvious bi-modal distribution, mainly concentrating around 16+ and/or 10+. In Groups A and B, their distributions appear around 16+ and 10+ at different intervals, with undulating variation fluctuating with the $\langle Q \rangle_{\text{Fe}}$ trend. Note that if just one or a few discrete $\langle Q \rangle_{\text{Fe}}$ data points are lower/higher than 12+, i.e., their surroundings are higher/lower than 12+, the discrete ones will be disregarded. In Group C/D, most of the distributions are mainly characterized by charge-state concentration around 16+/10+, consistent with their $\langle Q \rangle_{\text{Fe}}$ keeping higher/lower than 12+. This confirms that the 12+ condition is indeed an efficient identifier for separating the MC events with high or normal Fe charge states (Lepri & Zurbuchen 2004). It is of some importance for relevant studies, as the SWICS on board ACE suffered a hardware anomaly in 2011 and only $\langle Q \rangle_{\text{Fe}}$ data are available since then. Note that one or a few

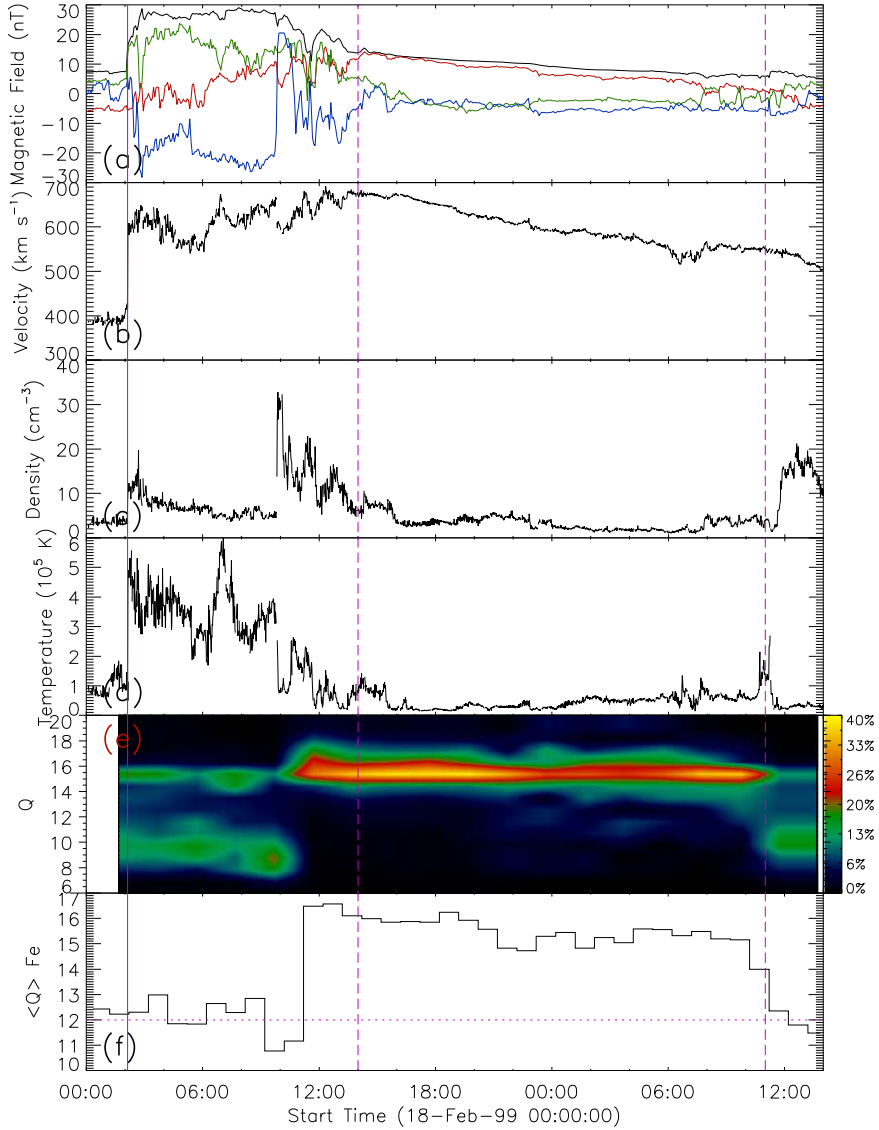


Figure 5. Same as Figure 3, but for the 19990218 event in Group C.

discrete data points in Group C/D are below/beyond 12+ (see the notes in Table 1 and the corresponding panels in Figure 7), which are disregarded, as mentioned above. Two events (20020420 and 20050520) in Group C have five continuous data points (less than 22% of their total data points) lower than 12+ near one boundary, while they do not noticeably change the $\langle Q \rangle_{\text{Fe}}$ distribution characteristics and are also neglected.

As mentioned above, most MCs ($\sim 96\%$) can be divided into Groups A–D. Four events cannot be classified into these groups and are included in Group E. We will discuss possible explanations for all groups in the next section.

4. DISCUSSION

In general, ICMEs can either exhibit high Fe charge states or not. Lynch et al. (2011) derived the ionic charge-state composition distribution using axisymmetric MHD simulations of CMEs initiated via either flux-cancellation or a magnetic breakout mechanism. They concluded that enhanced heavy ionic charge states within the flux rope are a direct consequence of flare heating in the lower corona, and not due to the heating of breakout reconnection. This is reasonable, since the breakout

reconnection mainly removes the constraint of overlying loops to trigger the eruption without adding new layers to the flux rope (Antiochos et al. 1999). Lepri & Zurbuchen (2004) suggested that magnetic connectivity in the part of the ICME observed in situ to the flaring region is the key to the presence of high Fe charge states. Here, we propose a different scenario.

According to the CME model (Forbes & Acton 1996; Lin & Forbes 2000; Lin et al. 2004), the flux rope and the flare region can be related with each other through the reconnecting current sheet in the wake of a CME. The Fe ions with high/normal charge states can be generated in the high/normal temperature current sheet (e.g., Ciaravella et al. 2013), in addition to the flare region, and fill in the corresponding layers of the flux rope like “layers of an onion,” as mentioned in Ko et al. (2013). In this paper, the high/normal temperature in the current sheet is defined as it is beyond/below 2 MK. This is consistent with the early calculation of Arnaud & Raymond (1992), which showed that high Fe charge states ($\geq 15+$) can have a considerable amount ($> 30\%$) above 2 MK. We point out that the temperature of a flux rope will likely decrease with its expansion when propagating outward; therefore, the $\langle Q \rangle_{\text{Fe}}$

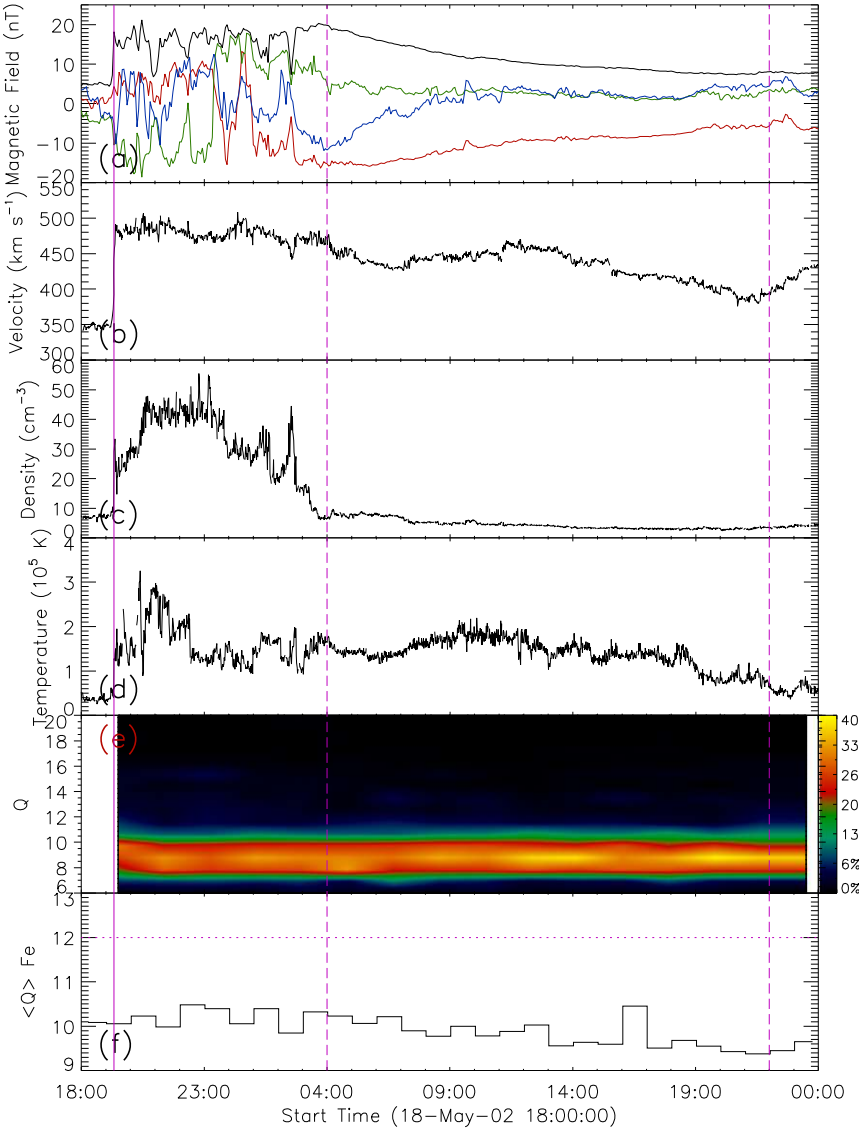


Figure 6. Same as Figure 3, but for the 20020519 event in Group D.

within the flux rope when reaching the charge-state freezing distance may not be as high as that in the earlier reconnecting current sheet region (e.g., Rakowski et al. 2007; Ko et al. 2010). Based on these points, we present our understanding of the above observations in Figure 8 with some schematics.

The left panels show the eruption with a pre-existing flux rope as delineated with a yellow circle filled with blue, which means its $\langle Q \rangle_{\text{Fe}}$ is lower than 12+. The large purple circle depicts the boundary of the MC. In panel (a1), the current sheet has a high temperature; this leads the $\langle Q \rangle_{\text{Fe}}$ to be higher than 12+, as depicted in red. Since the ionic charge states are mostly frozen before they leave the corona (e.g., Rakowski et al. 2007; Ko et al. 2010), the measured MC will likely contain a low/high ionized center/shell. If the spacecraft passes through the MC along the upper green arrow, a bimodal distribution like Figure 3(f) will be detected. If the spacecraft passes through the MC shell portion along the lower arrow, a distribution shape as pointed with the arrow should be observed, similar to Figure 5(f). Panel (a2) describes the case in which the current sheet temperature is high at first, but subsequently becomes

normal during the flux rope formation. Then the MC will contain a high-ionization-state inner shell and a low-ionization-state outer shell. The obtained $\langle Q \rangle_{\text{Fe}}$ shapes can be similar to Figures 3(f) or 4(f), depending on the spacecraft passage. It is also possible to get a distribution shape similar to Figure 6(f) if the spacecraft just passes through the MC edge, which is not plotted in panel (a2). Panel (a3) describes the case in which the current sheet temperature is normal during the flux rope growth. Then no Fe ions with high charge states are available to fill in the flux rope, which results in a distribution shape like that in Figure 6(f), no matter where the spacecraft passes through the MC.

The right panels present the scenario where the flux rope is formed during the eruption, so just a large purple circle is plotted at the MC boundary. Correspondingly, the top, middle, and bottom panels refer to cases in which the current sheet temperature is high, high then normal, and normal during the flux rope formation. It is easy to see that three $\langle Q \rangle_{\text{Fe}}$ distribution shapes can be obtained, except the bimodal distribution as shown in Figure 3(f). Therefore, our analysis suggests that the flux rope exists prior to the eruption if its MC

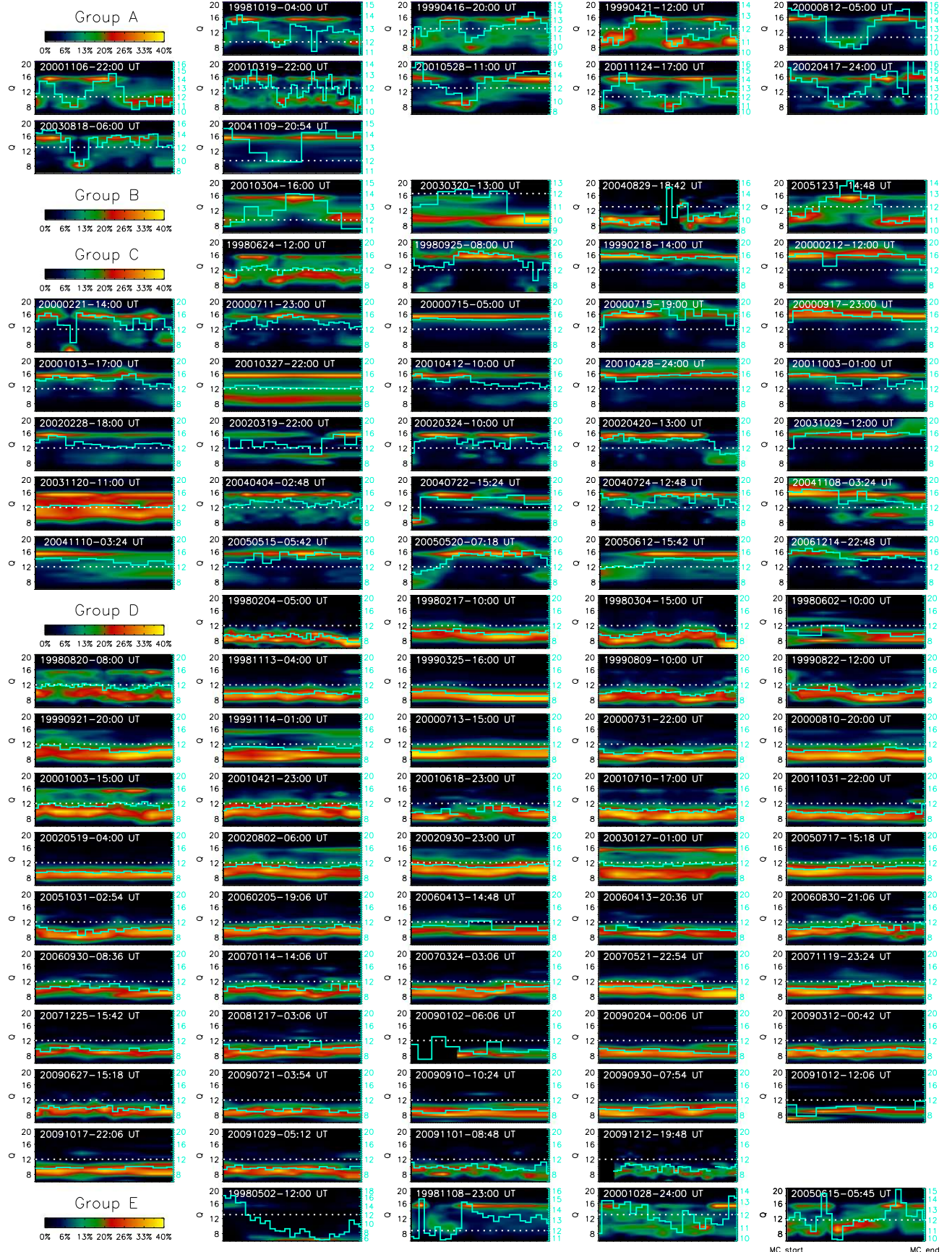


Figure 7. Fe charge-state distributions and $\langle Q \rangle$ Fe variations (cyan) within 96 MCs. The horizontal white dotted lines mark the level of 12+ for $\langle Q \rangle$ Fe. Groups A, B, C, and E are all associated with lots of high Fe charge states, while Group D is mainly associated with normal Fe charge states with $\langle Q \rangle$ Fe below 12+. The left/right boundary corresponds to each MC start/end time. See the text for details.

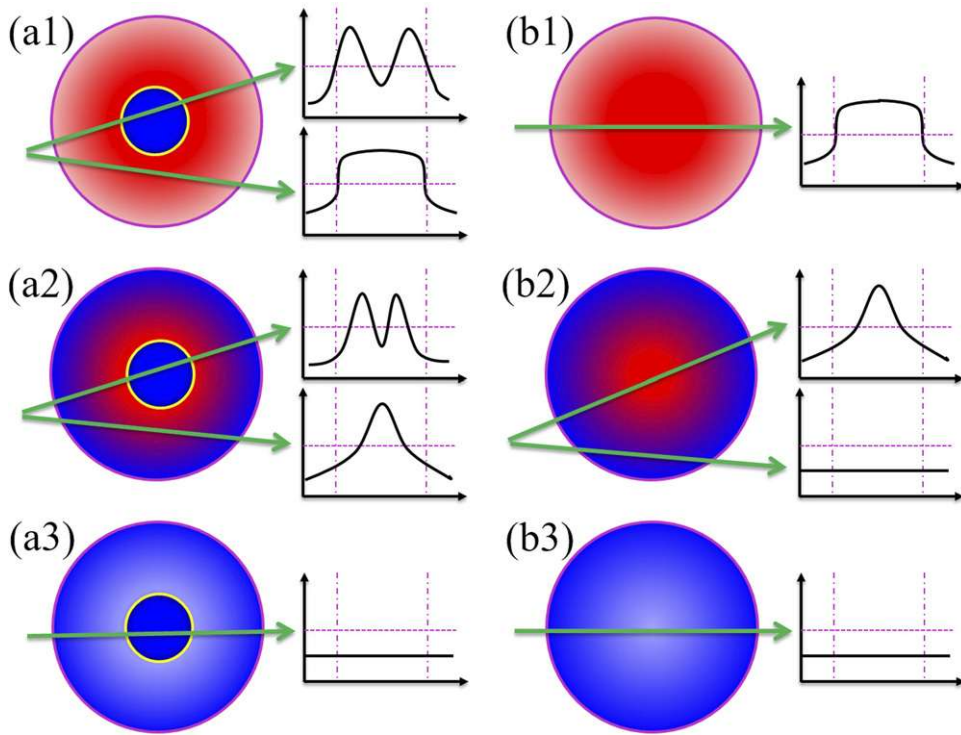


Figure 8. Schematic drawings of the explanation for the $\langle Q \rangle \text{Fe}$ distributions inside MCs. Red/blue denotes the $\langle Q \rangle \text{Fe}$ being higher/lower than 12+. The horizontal dotted lines in the coordinates mark the $\langle Q \rangle \text{Fe}$ level of 12+, and the purple vertical dot-dashed lines demarcate the MC boundaries. See the text for details.

$\langle Q \rangle \text{Fe}$ distribution presents the bimodal shape. In summary, the observed $\langle Q \rangle \text{Fe}$ distributions depend on how the spacecraft crosses the MC, and the physical properties of the flux rope and the current sheet near the Sun.

In order to support the above scenario, we checked the source regions of 11 CMEs in Group A with EIT on board the *Solar and Heliospheric Observatory* and H α images from the Big Bear Solar Observatory. The results show that seven (Events 1–6 and 8) of them are associated with filaments. This indicates a pre-existing flux rope (Rust & Kumar 1994; Song et al. 2015a) and supports our scenario. We cannot identify the source region for Event 7, and no filaments were observed in the source active regions for Events 9–11. It is not easy to confirm or deny the existence of other proxies of flux ropes prior to the eruptions, such as sigmoid structures (Titov & Démoulin 1999) and/or hot channels (Zhang et al. 2012; Song et al. 2015b), as no soft X-ray and high temperature EUV observations are available.

As mentioned above, some disagreements on the MC boundary locations often exist among different MC lists (e.g., Huttunen et al. 2005). To assess its influence on our statistical results, we checked another MC list (http://wind.nasa.gov/index_WI_ICME_list.htm) on the *WIND* website. Since *WIND* has been located at the L1 point since 2004, we mainly compared the 31 MCs that appeared both in this list and our Table 1 between 2004 and 2009. The difference between their start/end times varies on a range of 0~5.5/0.5~16.3 hr, with the average value being 1.7/4.5 hr, while the average MC duration across the spacecraft is close to 20 hr (e.g., Wu & Lepping 2011, 2015). According to this MC list, only 1 event (20050612) of the 31 MCs should be reclassified and moved from Group C to B. This almost does not affect our statistics.

Considering the complex dynamical processes of magnetic reconnection and CME eruption, as well as the propagation of a

flux rope in interplanetary space, not all $\langle Q \rangle \text{Fe}$ distributions are regular inside MCs and can be classified into Groups A–D. Four such events (Group E) are found, indicating that some complicated cases may exist. For example, when cold filament materials contained in MCs are detected in situ (Gloeckler et al. 1999; Lepri & Zurbuchen 2010), the $\langle Q \rangle \text{Fe}$ will descend and the charge-state distribution will change accordingly. The first event in Group E is probably such a case (Gloeckler et al. 1999), in which the $\langle Q \rangle \text{Fe}$ descends gradually from 16+ to 6+. The second event is odd, with the former/later part lower/higher than 12+ if the two discrete points beyond 12+ were neglected, and the remaining two events showing three peaks higher than 12+ inside the MCs. These events cannot be explained with our simple and qualitative scenario.

We also note some high Fe charge states exist outside the MCs, e.g., the sheath region in Figure 5(e). They might be generated by processes such as the breakout reconnection or heating of a lower coronal shock. They may also correspond to the outermost part of the magnetic flux rope in the corona, but are not regarded as parts of MCs possibly because of their irregular magnetic structure as measured in situ. For the high Fe charge states in ICMEs without an embedding MC, we speculate that they may also be produced by magnetic reconnection along the post-CME current sheet, yet the ejecta does not evolve into a regular MC structure.

5. SUMMARY

We performed a comprehensive survey of $\langle Q \rangle \text{Fe}$ distributions inside 96 MCs for solar cycle 23 using *ACE* data. The high Fe charge state is defined as when the $\langle Q \rangle \text{Fe}$ is larger than 12+, which means that a considerable amount of Fe ions with high charge states (e.g., $\geq 16+$) appear inside the MCs. The statistical results show that the distribution of 92 MCs (~96%)

can be classified into four groups with different characteristics. Group A (11 MCs) is defined as when the $\langle Q \rangle$ Fe shows a bimodal distribution with double peaks higher than 12+. Group B (4 MCs) presents a unimodal distribution with a peak higher than 12+. Groups C (29 MCs) and D (48 MCs) are defined by $\langle Q \rangle$ Fe always remaining higher and lower than 12+ during ACE's passage through the MC, respectively.

A qualitative scenario was proposed to explain the results, which can be used to infer the magnetic flux rope formation time and the current sheet temperature information during eruption. The high/normal Fe charge state indicates that the current sheet temperature is high/normal during the eruption, and the bimodal distribution exists only if the flux rope has been formed prior to the eruption. Our study supports this scenario in a preliminary and statistical way. More detailed case studies are needed to further test this scenario.

We are grateful to the referee for his/her constructive comments and suggestions, which improved the paper greatly. We thank Susan T. Lepri, Lan Jian, Jun Lin, Yuming Wang, Pengfei Chen, Yong Liu, and Chenglong Shen for their valuable comments and discussion. We acknowledge the use of data from the ACE and WIND missions. This work is supported by the 973 program 2012CB825601, NNSFC grants 41274177, 41274175, and 41331068. J.Z. is supported by US NSF AGS-1249270 and NSF AGS-1156120. G.L. is supported by ATM-0847719 and AGS-1135432. The work of L.Z. is supported by NSF grants AGS-1432100 and AGS-1344835.

REFERENCES

- Antiochos, S. K., Devore, C. R., & Klimchuk, J. A. 1999, *ApJ*, **510**, 485
 Arnaud, M., & Raymond, J. 1992, *ApJ*, **398**, 394
 Bemporad, A., Poletto, G., Suess, S. T., et al. 2006, *ApJ*, **638**, 1110
 Burlaga, L., Sittler, E., Mariani, F., & Schwenn, R. 1981, *JGR*, **86**, 6673
 Chen, J. 1996, *JGR*, **101**, 27499
 Cheng, X., Ding, M. D., Zhang, J., et al. 2014, *ApJ*, **789**, 93
 Cheng, X., Zhang, J., Ding, M. D., Liu, Y., & Poomvises, W. 2013, *ApJ*, **763**, 43
 Chi, Y., Shen, C., Wang, Y., Ye, P., & Wang, S. 2015, arXiv:1504.07849
 Ciaravella, A., Webb, D. F., Giordano, S., & Raymond, J. C. 2013, *ApJ*, **766**, 65
 Forbes, T. G., & Acton, L. W. 1996, *ApJ*, **459**, 330
 Gloeckler, G., Cain, J., Ipavich, F. M., et al. 1998, *SSRv*, **86**, 497
 Gloeckler, G., Fisk, L. A., Hefti, S., et al. 1999, *GeoRL*, **26**, 157
 Gopalswamy, N. 2006, *SSRv*, **124**, 145
 Gosling, J. T., McComas, D. J., Phillips, J. L., & Bame, S. J. 1991, *JGR*, **96**, 7831
 Gruesbeck, J. R., Lepri, S. T., Zurbuchen, T. H., & Antiochos, S. K. 2011, *ApJ*, **730**, 103
 Hu, Q., & Sonnerup, B. U. Ö 2002, *JGRA*, **107**, 1142
 Huttunen, K. E. J., Schwenn, R., Bothmer, V., & Koskinen, H. E. J. 2005, *AnGeo*, **23**, 625
 Jian, L., Russell, C. T., Luhmann, J. G., & Skoug, R. M. 2006, *SoPh*, **239**, 393
 Kilpua, E. K. J., Isavnin, A., Vourlidas, A., Koskinen, H. E. J., & Rodriguez, L. 2013, *AnGeo*, **31**, 1251
 Ko, Y.-K., Raymond, J. C., Rakowski, C., & Rouillard, A. 2013, in AIP Conf. Ser. 1539, SOLAR WIND 13: Proc. Thirteenth Int. Solar Wind Conf., ed. G. P. Zank et al. (Melville, NY: AIP), 207
 Ko, Y.-K., Raymond, J. C., Vršnak, B., & Vujić, E. 2010, *ApJ*, **722**, 625
 Lepping, R. P., Berdichevsky, D. B., Wu, C. C., et al. 2006, *AnGeo*, **24**, 215
 Lepping, R. P., Burlaga, L. F., & Jones, J. A. 1990, *JGR*, **95**, 11957
 Lepping, R. P., & Wu, C. C. 2010, *AnGeo*, **28**, 1539
 Lepping, R. P., Wu, C.-C., & Berdichevsky, D. B. 2015, *SoPh*, **290**, 553
 Lepping, R. P., Wu, C.-C., Berdichevsky, D. B., & Szabo, A. 2011, *SoPh*, **274**, 345
 Lepri, S. T., Laming, J. M., Rakowski, C. E., & von Steiger, R. 2012, *ApJ*, **760**, 105
 Lepri, S. T., & Zurbuchen, T. H. 2010, *ApJL*, **723**, L22
 Lepri, S. T., & Zurbuchen, T. H. 2004, *JGRA*, **109**, A01112
 Lepri, S. T., Zurbuchen, T. H., Fisk, L. A., et al. 2001, *JGR*, **106**, 29231
 Lin, J., & Forbes, T. G. 2000, *JGR*, **105**, 2375
 Lin, J., Raymond, J. C., & van Ballegooijen, A. A. 2004, *ApJ*, **602**, 422
 Lynch, B. J., Reinard, A. A., Mulligan, T., et al. 2011, *ApJ*, **740**, 112
 McComas, D. J., Bame, S. J., Barker, P., et al. 1998, *SSRv*, **86**, 563
 Mikić, Z., & Linker, J. A. 1994, *ApJ*, **430**, 898
 Ouyang, Y., Yang, K., & Chen, P. F. 2015, *ApJ*, **815**, 72
 Patsourakos, S., Vourlidas, A., & Stenborg, G. 2013, *ApJ*, **764**, 125
 Rakowski, C. E., Laming, J. M., & Lepri, S. T. 2007, *ApJ*, **667**, 602
 Rust, D. M., & Kumar, A. 1994, *SoPh*, **155**, 69
 Shearer, P., von Steiger, R., Raines, J. M., et al. 2014, *ApJ*, **789**, 60
 Smith, C. W., L'Heureux, J., Ness, N. F., et al. 1998, *SSRv*, **86**, 613
 Song, H. Q., Chen, Y., Zhang, J., et al. 2015a, *ApJL*, **804**, L38
 Song, H. Q., Chen, Y., Zhang, J., et al. 2015b, *ApJL*, **808**, L15
 Song, H. Q., Zhang, J., Chen, Y., & Cheng, X. 2014a, *ApJL*, **792**, L40
 Song, H. Q., Zhang, J., Chen, Y., et al. 2015c, *ApJ*, **803**, 96
 Song, H. Q., Zhang, J., Cheng, X., et al. 2014b, *ApJ*, **784**, 48
 Titov, V. S., & Démoulin, P. 1999, *A&A*, **351**, 707
 von Steiger, R., Schwadron, N. A., Fisk, L. A., et al. 2000, *JGR*, **105**, 27217
 Wang, Y., Zhou, Z., Shen, C., Liu, R., & Wang, S. 2015, *JGRA*, **120**, 1543
 Wu, C.-C., & Lepping, R. P. 2011, *SoPh*, **269**, 141
 Wu, C.-C., & Lepping, R. P. 2015, *SoPh*, **290**, 1243
 Zhang, J., Cheng, X., & Ding, M.-D. 2012, *NatCo*, **3**, 747
 Zhang, J., Dere, K. P., Howard, R. A., & Bothmer, V. 2003, *ApJ*, **582**, 520
 Zhang, J., Richardson, I. G., Webb, D. F., et al. 2007, *JGRA*, **112**, A10102